Supplementary material: Weakening of the pinning point buttressing Thwaites Glacier, West Antarctica

by Christian T. Wild, Karen E. Alley, Atsuhiro Muto, Martin Truffer, Ted A. Scambos, Erin C. Pettit
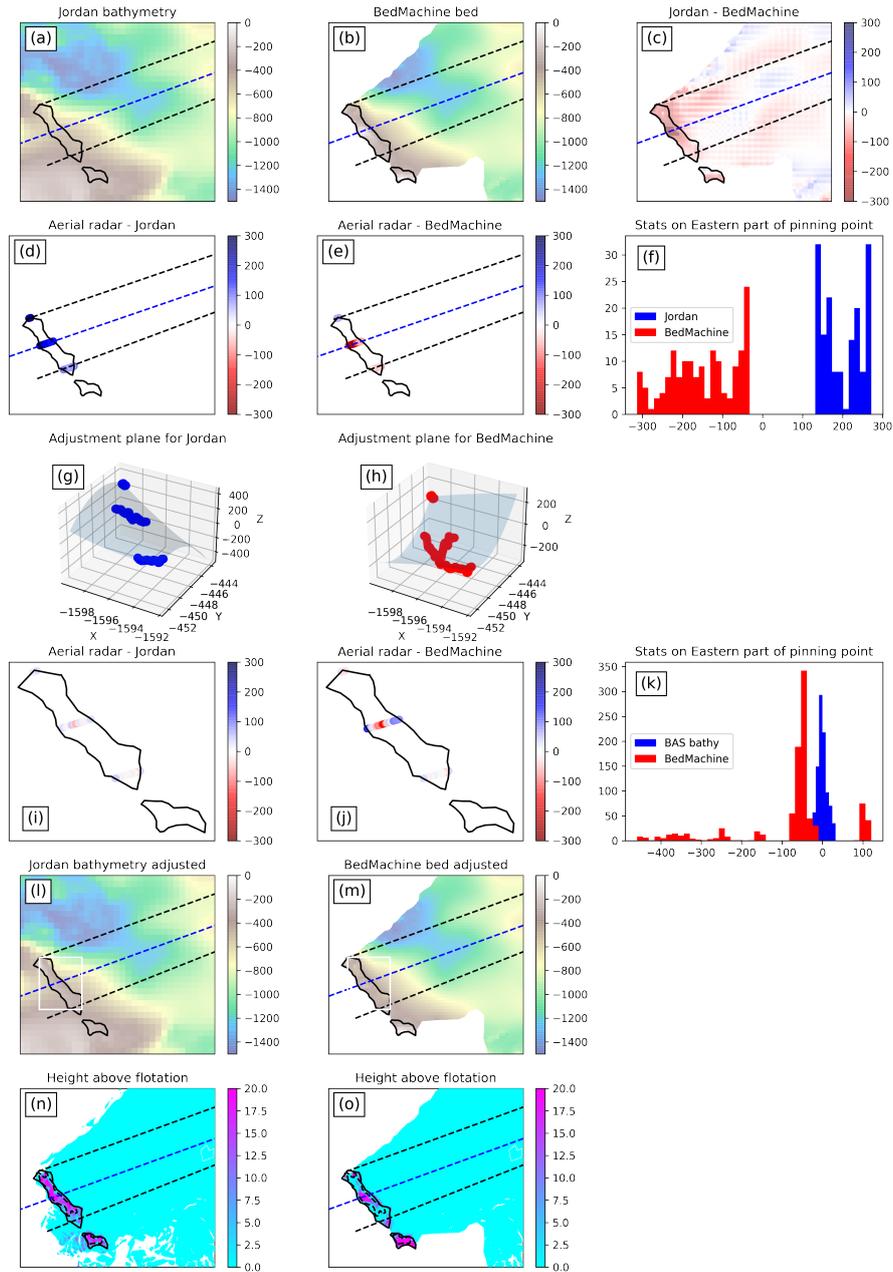
Figure S1. Adjustment of the pinning point bathymetry to match airborne radar data where ice is locally grounded on the seafloor. The adjustment is performed for the Jordan bathymetry and the BedMachine v2 data. (a) to (c) shows the published bathymetry and their differences. Panels (d) to (f) show their differences to ice thicknesses as measured using airborne radar, and statistics thereof. Panels (g) and (h) show the adjustment planes that were fitted through these differences. (i) to (k) shows the differences after the adjustment and statistics thereof. Panels (l) and (m) show the now adjusted bathymetry maps that are constrained with airborne radar measurements across the Eastern portion of the pinning point. (n) and (o) show height above flotation calculations using the two adjusted bathymetry maps. Blue dashed line shows the location of the 2009 radar transect, the black dashed line the two transects crossing the edges of the pinning point in 2019.
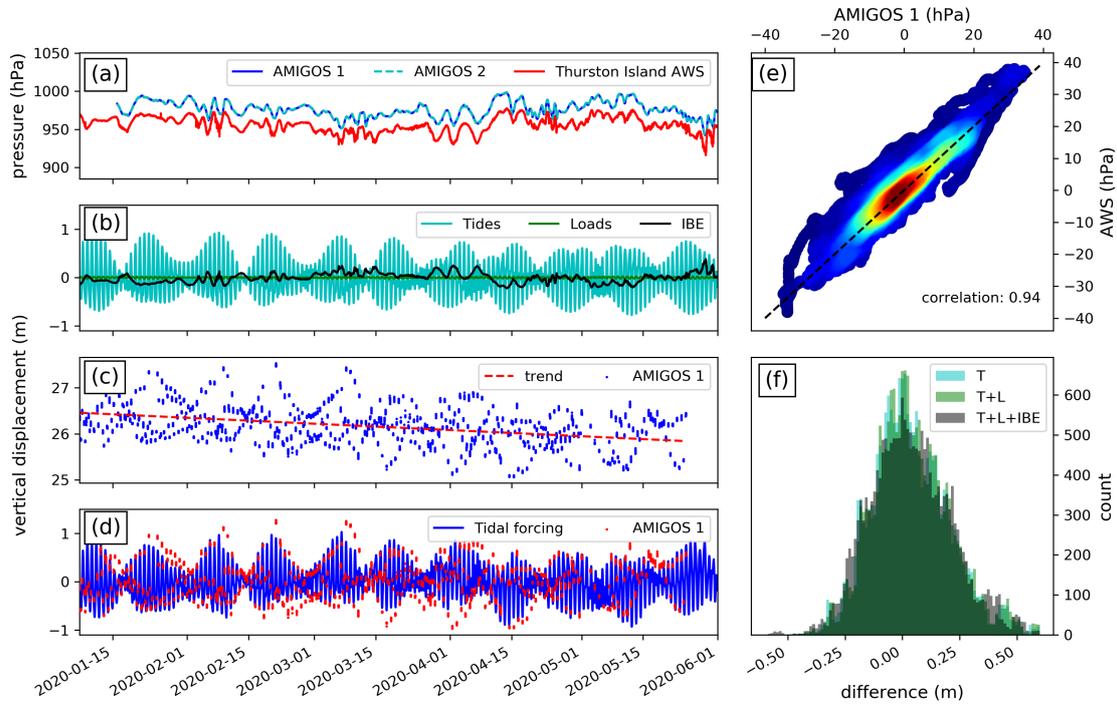
Figure S2. Uncertainty analysis on tide correction of kinematic GPS and ICESat-2 data: (a) Barometric pressure measured with two AMIGOS on Thwaites Eastern Ice Shelf and a nearby automatic weather station on Thurston Island. (b) Scatter plot between local and remote pressure anomalies. (c) Oceanic Tides as predicted by the CATS2008 model, load tides as predicted by TPXO9 model and the inverse barometric effect as calculated from pressure anomalies of the weather station data. (d) Detrended 3 hourly GPS measurements on the Eastern Ice Shelf in comparison to the modeled tidal forcing. (e) Scatter plot between barometric pressure anomalies at the Eastern Ice Shelf compared to the Thurston Island AWS, colour-coded by point density. (f) Histogram of the differences between modelled and measured vertical displacements for tides only (T), tides plus load tides (T+L) and tides, loads, and the inverse barometric effect (IBE).
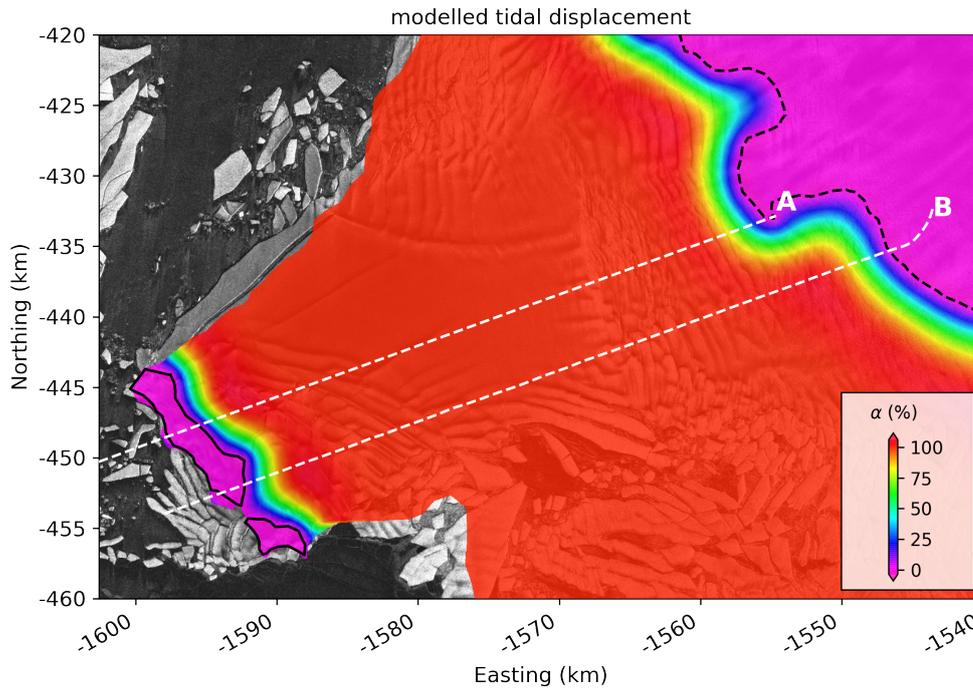
Figure S3. α-map of percentage tidal displacement as calculated using an elastic finite-element model showing (red) freely-floating areas synchronous with the tidal oscillation and (purple) completely grounded areas outside the reach of vertical tidal forcing. The dashed white lines show the locations of airborne radar surveys (A) in 2009 and (B) January 2019. The dashed black line marks the location of the 2017 grounding line, the solid black line marks the 2011 grounding line on Thwaites pinning point.
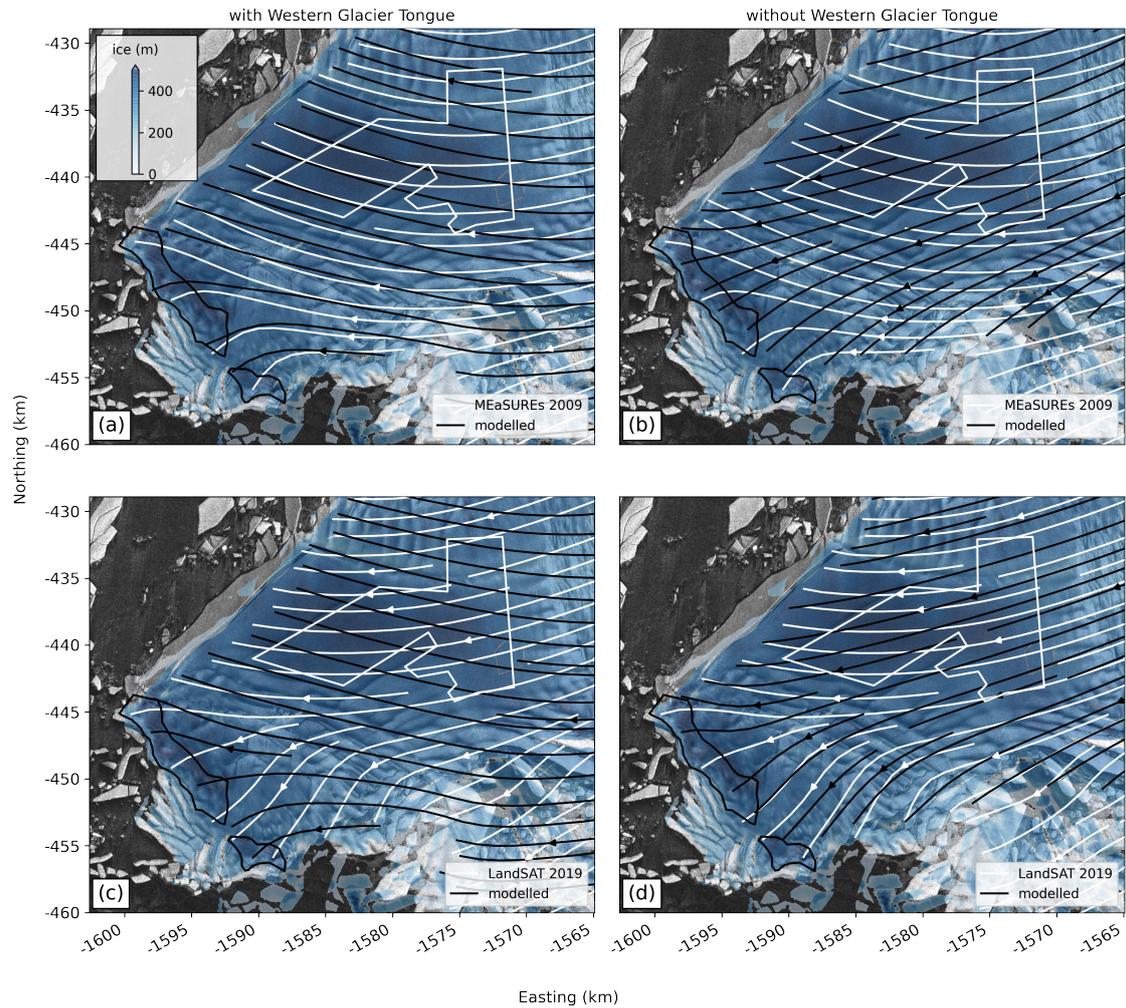
Figure S4. Comparison between (white) satellite derived streamlines and (black) numerical solutions from ISSM: (a) The situation before the break-up of Western Glacier Tongue in 2009 with a relatively well-grounded pinning point. (b) Removal of the Western Glacier Tongue causing anti-clockwise rotation of ice flow in the modeled solution. (c) Replacing the MEaSUREs velocity field with recent Landsat-8 data, while keeping the full extent of the Western Glacier Tongue, misses both the observed anti-clockwise rotation of ice flow and the ice funneling between the two remaining portions of the pinning point as observed in the satellite data. (d) Removing the Western Glacier Tongue from the model domain, and thus weakening its influence on the Eastern Ice Shelf, reproduces both observed ice-dynamical changes. Blue colors correspond to the ice thickness estimate derived in this study.
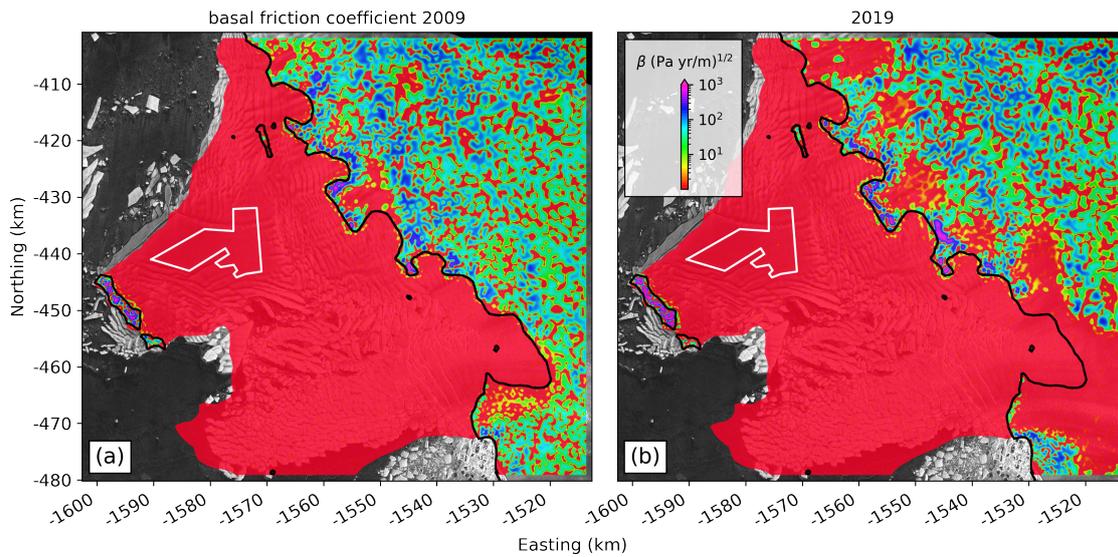
Figure S5. Basal friction coefficient fields derived from (a) MEaSUREs 2009 and (b) Landsat-8 2019 which minimize the misfit between observed and modeled ice velocities using the 2011 grounding line.
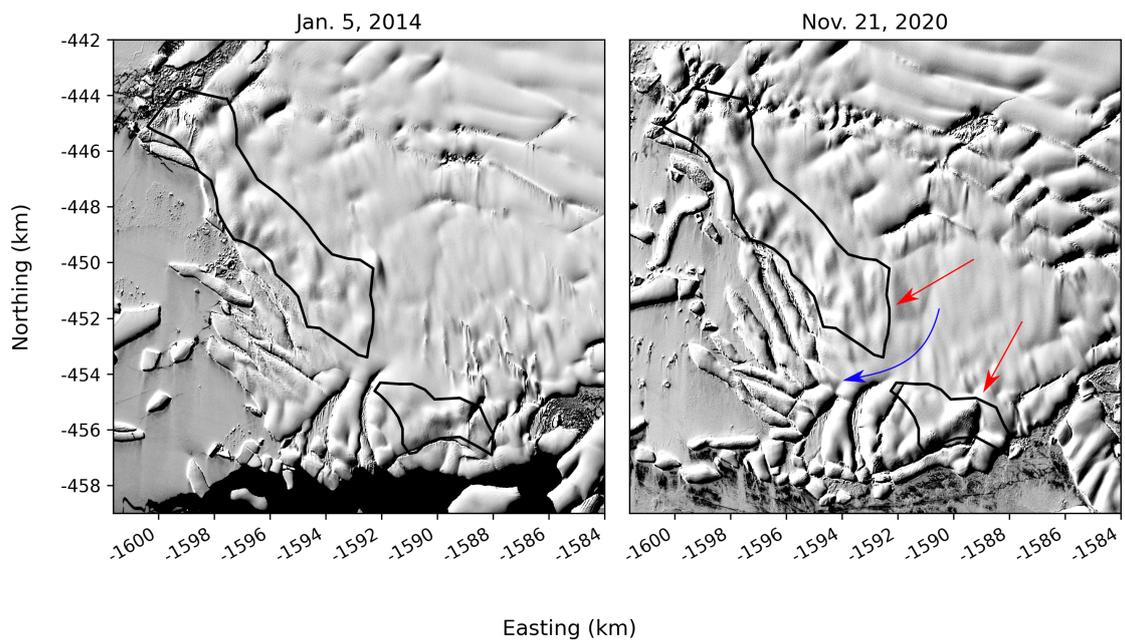
Figure S6. Contrast-stretched, panchromatic Landsat imagery of the pinning point area. The black line corresponds to the 2011 grounding line. Note the increased ice funneling between the two portions of the pinning point (blue arrow), and areas of local weakening (red arrows).